# A Dual-Side Magnetic Integration–Based Receiver Detection Method of Long-Track DWPT System

Junhua Wang, *Member, IEEE*, Leke Wan, Changsong Cai, *Senior Member, IEEE*, Ming Xue, Yinfeng Du, and Jin Zhang

***Abstract*—Position detection of the energy pickup receiver (Rx) in long-track dynamic wireless power transfer (DWPT), including longitude misalignment and motion trace, is essential for practical applications. This article presents a dual-side magnetic integration-based Rx position detection (RPD) method, which utilizes integrated inductor coils of the *LCC-LCC* compensated DWPT topology to achieve cost-effective Rx detection without extra sensors or energizing circuits. Solenoid and bipolar integrated coils are, respectively, designed in the transmitter and Rx sides to realize Rx detection without affecting WPT performance. Key parameters of the integrated coils are optimized for accurate Rx positioning. The Rx detection strategy is then developed based on two mapping indicators, holding the merits of dual-objective Rx detection capabilities and a simplified positioning procedure. A scaled-down long-track DWPT experimental prototype is established to demonstrate the effectiveness and feasibility of the proposed RPD method under dynamic operation or malfunction conditions. The experimental results show that a reasonable sampling interval can mitigate the positioning error caused by the vehicle's velocity.**

***Index Terms*—Dual-side magnetic integration, longitude misalignment, long-track dynamic wireless power transfer (DWPT), motion trace, receiver (Rx) position detection (RPD).**

## I. Introduction

AUTOMATIC vehicles are often assigned the responsibility of material handling tasks along pre-established routes in some industrial settings, as shown in Fig. 1 [1], [2], [3]. When the battery capacity of these vehicles is depleted, they are required to halt at authorized charging stations, impairing the plant's overall operational efficiency. To tackle this challenge, dynamic wireless power transfer (DWPT) has opened new possibilities for multiple vehicles' wireless charging [4], [5], [6], [7]. Specifically, the use of integrated array coils or segmented coils has been applied to charge multiple vehicles [8], [9]. However, substantial segmented coils might result in notable expense escalation and heightened intricacy in control. Long-track DWPT system, formerly referred to as the lumped inductive power transfer system, targeting supplying power to trains or moving electric vehicles (EVs) that travel in a designated route, is relatively lower cost and more convenient [10], [11].

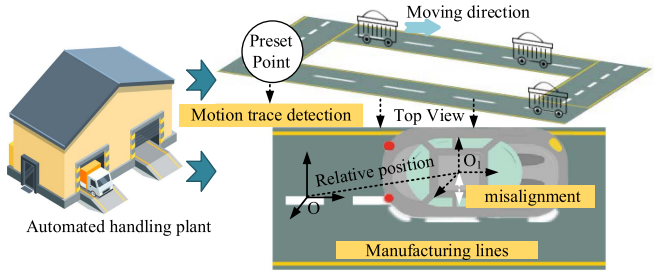


Fig. 1. Application scenario of automatic vehicles and their working conditions.

Longitude misalignment of the receiver (Rx) off the predetermined route, as illustrated in Fig. 1, may occur during the operation process due to accidental collisions or navigation system errors, which may disturb the transfer performance of the long-track DWPT system [12]. The motion trace detection of automatic vehicles entails the monitoring of how many times a vehicle passes preset trajectory points along the transmitter (Tx) track, facilitating an assessment of its operational status and the need for scheduled maintenance. Yet the traditional method for the installation of counting sensors may be susceptible to external interference. Therefore, realization for Rx position detection (RPD) includes longitude misalignment and motion trace detection, accompanied by the long-track DWPT system, promising significant potential.

The current research on the RPD method in dynamic wireless charging primarily centers around the positioning method itself [13], [14], [15], [16], [17], [18], [21], [22], [23], [24], [25], [26], [27], [28]. However, there is a limited number of studies that emphasized the practical application of a specific DWPT system [19], [20], which motivates this study.

The prior references install several sensors or auxiliary circuits to detect the Rx position, such as GPS, RFID tracker, antenna array, and TMR sensors [13], [14], [15], [16], [17], [18], but these methods may be interfered by the external environment factors and usually feature costly implementation. To address

Manuscript received 15 November 2023; revised 25 January 2024; accepted 24 February 2024. Date of publication 12 March 2024; date of current version 19 April 2024. This work was supported by the National Natural Science Foundation of China under Project 5207013. Recommended for publication by Associate Editor M. Ponce-Silva. *(Corresponding author: Changsong Cai.)*

Junhua Wang, Leke Wan, Changsong Cai, Yinfeng Du, and Jin Zhang are with the Hubei Key Laboratory of Power Equipment & System Security for Integrated Energy, School of Electrical Engineering and Automation, Wuhan University, Wuhan 430072, China, and also with the School of Electrical Engineering and Automation, Wuhan University, Wuhan 430072, China (e-mail: junhuawang@whu.edu.cn; lekewan@whu.edu.cn; changsongcai@whu.edu.cn; yinfengdu@whu.edu.cn; 2021282070149@whu.edu.cn).

Ming Xue is with the State Key Laboratory of Reliability and Intelligence of Electrical Equipment, Hebei University of Technology, Tianjin 300401, China (e-mail: xueming@hebut.edu.cn).

Color versions of one or more figures in this article are available at https://doi.org/10.1109/TPEL.2024.3374825.

Digital Object Identifier 10.1109/TPEL.2024.3374825

this issue, electromagnetic characteristics of the wireless power transfer (WPT) system is being studied and utilized to detect the Rx [18], [19], [20], [21], [22], [23], [24], [25], [26], [27], [28], [29]. Multiple ferrites are placed beneath the long-track source coil [18], where the position of the mobile Rxs is detected by counting the number of the traversed ferrite strips. A comprehensive gauging method by setting up a mathematical relationship between Tx side circuit parameters and mutual inductance (MI) is proposed [22], [23]. However, the stable MI region is limited, and threshold point discussion is not covered, reducing its real-world practicality. A dual-side interactive RPD method with a vehicle-side pulse is proposed [22]. The presented detection approach avoids the response delay between the trigger pulses and the start-up of power transmission. However, the vehicle-mounted GPS is necessary for the start of the detection process. To reduce costs brought by the sensors or other positioning devices, the auxiliary coils' positioning method is exhibited [23], [24], in which the induced voltage at each effective localization point is accumulated, allowing for the detection of the relative position by searching the pre-established voltage lookup table.

Researchers have also explored the configuration scheme, magnetic integration design, and nested assembly of the auxiliary coils to realize low integration complexity and cost-effective Rx positioning [25], [26], [27], [28], [29]. A coordinate positioning technique based on region partitioning for determining the relative position between the Tx and Rx coils as well as the correct moving direction of the Rx coil is proposed in [25]. Three Tx coils are connected in parallel at the Tx end, each controlled by an independent switch, ensuring no interference among them. Zhang et al. [26] proposed a triple-coil-based positioning approach, by which the RPD with a low electromagnetic field is achieved by orderly exciting the sensing coil. A decoupled nested transformer with an integrated solenoid coil and bipolar coil is constructed [27], in which the coupling coefficient is assigned as a mapping indicator for misalignment detection. The combination of bipolar and unipolar configurations eliminates mutual cross-coupling effects. However, the use of two sets of inverters for power supply results in increased costs. A WPT system for detecting misalignment in EVs is developed using two orthogonal detector (Dx) coils [28]. The two auxiliary coils need extra energizing circuits and multichannel multiplexer for signal routing, which increases the overall cost and makes the positioning process complex. Four magnetic integration square inductor coils with specific connection sequences are assigned for Rx detection [29]. This is achieved by monitoring the input current's voltage and current as well as the current injected into the Tx coil. The appointed polarity configuration decouples all four integrated coils from the Tx and Rx coils, resulting in an essential zero voltage switching condition.

Currently, existing positioning methods with auxiliary coils' implementation primarily focus on detection accuracy enhancement algorithm and nested magnetic coupler structure [24], [25], [26], [27], [28]. These studies introduce extra control switches or circuits to achieve Rx detection with auxiliary coils, which increases the positioning cost. Therefore, it is imperative to develop a cost-effective coil positioning method with a compact magnetic coupling structure, all while in line with the practical industrial operation requirements.

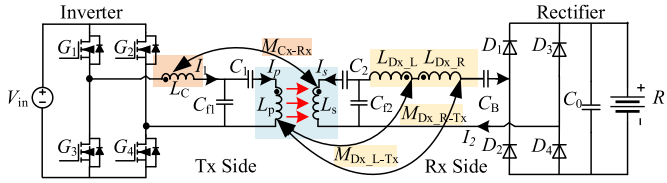


Fig. 2. Circuit diagram of the dual-side magnetic integration topology.

In this article, a pair of magnetic integration coils, cooperated with the double-sided inductor-capacitor-capacitor (*LCC*) compensation topology, is developed to enable cost-effective positioning detection in long-track DWPT systems, eliminating the need for additional sensors and realizing cost-effective positioning detection in industrial settings. Each coil is crafted for distinct position detection functions, detecting longitude misalignment and tracking the movement of mobile Rxs, all while without affecting WPT performance. The Tx side bridge inductance is integrated into a solenoid counter (Cx) coil, serving the purpose of counting the motion cycles of the Rx. Concurrently, the corresponding component integrated on the Rx side is partitioned into two unipolar Dx coils that are invertedly connected and serve the purpose of detecting longitude misalignment. Key structural parameters of the two types of coils are optimized, ensuring dynamic positioning within the effective detection range. The Rx detection strategy and corresponding process, based on the mapping indicators of deviation direction, misalignment amplitude, and passing preset trajectory points, are developed. In establishing the RPD strategy, the issue of excessive positioning errors caused by high speeds has been addressed by setting appropriate sampling intervals. The proposed coil positioning method employs a dual-side magnetic integration design, requiring no additional energizing circuits, sensors, and control switches, thereby reducing overall cost compared to those in [24], [25], [26], [27], [28], and [29].

The rest of this article is organized as follows. Section II presents the proposed dual-objective Rx detection method. In Section III, the integrated coils' design for dynamic Rx positioning is presented. Next, the dual-objective Rx detection strategy and the Rx rotation condition are given and analyzed. Experimental verification for the proposed Rx detection strategy and analysis of the various operational speeds is presented in Section V. Finally, Section VI concludes this article.

## II. Proposed Dual-Side Magnetic Integration–Based Rx Detection Method

### A. Overview of the Dual-Objective Rx Detection Method

The proposed dual-objective Rx detection method includes the detection of Rx deviation direction and longitude misalignment amplitude and the times Rx passes through the trajectory points, by which the Rx position information is obtained, thereby facilitating the plant operation efficiency.

Fig. 2 presents the circuit diagram of the proposed magnetic integration circuit design employing *LCC-LCC* compensation

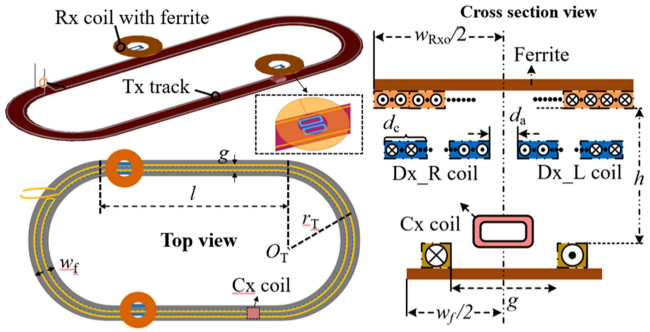


Fig. 3. Overall view of the physical coils in the long-track DWPT system.

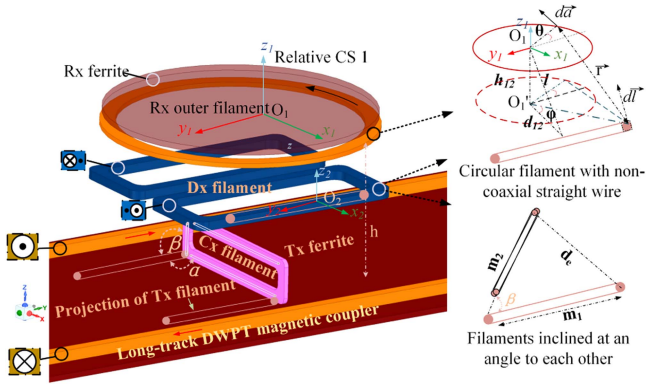


Fig. 4. Spatial MIs calculation using filament model with ferrites.

TABLE I
SYMBOLS AND MEANINGS IN THE LONG-TRACK DWPT SYSTEM

| Symbol | Physical meaning |
|---|---|
| $w_{\mathrm{Rxo}}$ | Width of the Rx ferrite |
| $w_{\mathrm{f}}$ | Width of the Tx track |
| $d_{\mathrm{a}}$ | Gap distance between the two Dx coils |
| $d_{\mathrm{c}}$ | Midsection coverage of the Dx coils |
| $g$ | Pitch width of the Tx coil |
| $l$ | Length of the straight track |
| $r_{\mathrm{T}}$ | Radius of the curved track |

topology. $L_{\mathrm{C}}$ represents the Cx coil, and $C_{\mathrm{f1}}$ and $C_1$ are the compensated capacitors on the Tx side. $L_{\mathrm{Dx\_L}}$ and $L_{\mathrm{Dx\_R}}$ are the two integrated bipolar coils that are reversely connected in a circuit, by which the MI values between these two Dx coils and other coils are the same in magnitude but opposite in sign, and therefore counteracting the related coupling. $C_{\mathrm{f2}}$ and $C_2$ are the Rx side compensation capacitors, and $C_{\mathrm{B}}$ is the balanced capacitor used for extra inductance value compensation of the Dx coils. The self-inductance of the Tx coil and Rx coil are expressed in symbols with $L_{\mathrm{P}}$ and $L_{\mathrm{S}}$. $V_{\mathrm{in}}$ is the dc input voltage before the full-bridge inverter and $R$ is the equivalent load of the vehicle. $M_{\mathrm{Cx\text{-}RX}}$, $M_{\mathrm{Dx\_L\text{-}Tx}}$, and $M_{\mathrm{Dx\_R\text{-}Tx}}$ are the MIs correlated to the coils which are represented in the subscript. $I_1$, $I_2$, $I_{\mathrm{p}}$, and $I_{\mathrm{S}}$ are the root-mean-square values of the input current of the inverter and rectifier, and the current flowing through Tx and Rx coils, respectively. These parameters are the key elements for attaining two mapping indicators for Rx detection.

Fig. 3 displays the overall view of the physical coils in this scaled-down long-track DWPT system [30]. The experimental prototype used in this article is identical to that in [30], albeit serving a distinct research objective. The crucial coil design parameters are shown in Table I. The integrated solenoid Cx coil and a pair of reversely connected bipolar Dx coils, which also serve as compensated inductors of the *LCC-LCC* topology, respectively, function as motion trace detection and distinguishing longitude misalignment direction and amplitude. An oval scaled-down Tx track is employed, in which the high-frequency currents flowing through the outer and inner windings exhibit different directions, hence enhancing the magnetic field strength above the Tx track.

The specific MI expressions depicted in Fig. 2 are utilized to establish two mapping indicators. The first indicator determines the longitude misalignment direction and magnitude, based on the MIs between the Dx coils and the Tx coil, denoted as $M_{\mathrm{Dx\_L\text{-}Tx}}$ and $M_{\mathrm{Dx\_R\text{-}Tx}}$. The second mapping indicator facilitates motion trace detection, achieved by calculating the real value of the MI between the Cx coil and the Rx coil, referred to as $M_{\mathrm{Cx\text{-}Rx}}$. In practical operation, the efficacy of the proposed RPD method hinges on the number of preset values of two mapping indicators. However, for safety reasons, it is crucial to implement an operational threshold which will be taken into discussion in Section III.

### B. Rx Detection Principle

The proposed dual-side magnetic integration design involves multiple MIs, some of these are crucial for Rx detection, whereas others are redundant. The two Dx coils are reversely connected in the circuit, and their MIs with Cx, Rx, and Tx coils can be described as follows:

$$M_{\mathrm{Dx-total}} = M_{\mathrm{Dx\_L-Cx}} + M_{\mathrm{Dx\_R-Cx}} + M_{\mathrm{Dx\_L-Rx}} + M_{\mathrm{Dx\_R-Rx}} + M_{\mathrm{Dx\_L-Tx}} + M_{\mathrm{Dx\_R-Tx}}. \tag{1a}$$

The Cx coil is constructed as a perpendicular type against the Tx track, and its MIs with Rx, Tx, and Dx coils can be deduced as follows:

$$M_{\mathrm{Cx-total}} = M_{\mathrm{Cx-Rx}} + M_{\mathrm{Cx-Tx}} + M_{\mathrm{Cx-Dx\_L}} + M_{\mathrm{Cx-Dx\_R}}. \tag{1b}$$

The presented MIs expressions encompass two types of spatial coupling relationships as illustrated in Fig. 4. $M_{\mathrm{Dx\_L\text{-}Rx}}$, $M_{\mathrm{Dx\_R\text{-}Rx}}$, and $M_{\mathrm{Cx\text{-}Rx}}$ belong to the type of circular filament with noncoaxial straight wire, and $M_{\mathrm{Dx\_L\text{-}Tx}}$, $M_{\mathrm{Dx\_R\text{-}Tx}}$, $M_{\mathrm{Dx\_L\text{-}Cx}}$, $M_{\mathrm{Dx\_R\text{-}Cx}}$ belong to the second type in the figure. The expression for calculating MI for the first type can be derived as

$$M = G_{\mathrm{Tx}} G_{\mathrm{Rx}} \int_0^{2\pi} \int_{-\varphi'}^{\varphi'} \frac{d_{12} \tan\varphi r \cos(90^\circ - \varphi) d\varphi d\theta}{\sqrt{r^2 + {p_e}^2 + 2 r p_e \sin(\theta - \varphi) + {h_{12}}^2}} \tag{2a}$$

TABLE II
SYMBOLS AND MEANINGS IN THE MI CALCULATION

| Symbol | Physical meaning |
|---|---|
| $\alpha$ | Angle between two filaments perpendicular to the XY-plane |
| $\beta$ | Angle between two filaments perpendicular to the XZ-plane |
| $\varphi$ | Angle between the circular filament center point and the straight filament integration part |
| $\theta$ | Angle between the integration part tangent vector and the center of the circle |
| $h_{12}$ | Vertical distance from the center of the straight filament to the center of the circular filament projection |
| $d_{12}$ | Distance from the center of the straight filament to the center of the circular filament projection |
| $m_1$ | Length of the first single filament |
| $m_2$ | Length of the second single filament |
| $d_e$ | Distance between the filament ends |

whereas the second type can be derived as [31]

$$M = 0.01 m_1 \cos\beta G_{T\times} G_{R\times} \left[ \ln \frac{1+\frac{m_1}{m_2}+\frac{d_e}{m_2}}{1-\frac{m_1}{m_2}+\frac{d_e}{m_2}} + \frac{m_1}{m_2} \ln \frac{\frac{m_1}{m_2}+\frac{d_e}{m_2}+1}{\frac{m_1}{m_2}+\frac{d_e}{m_2}-1} \right] \tag{2b}$$

where the physical meaning of the mentioned parameters are presented in Table II, and $G_{\mathrm{Tx}}$ and $G_{\mathrm{Rx}}$ are the linear field enhancement factors of the Tx and Rx ferrites.

It can be concluded that $M_{\mathrm{Dx\text{-}total}}$ remains zero from (2a) and (2b). The results from the bipolar and reverse connection characteristics of two Dx coils, where a pair of MIs generated by the Dx_L and Dx_R coils are opposite in sign but equal in amplitude.

The Cx coil is positioned perpendicularly to the Tx and the Dx coils in terms of their spatial relationship. As depicted in Fig. 4, this configuration results in $\beta$ being set at 90°, leading to the MIs related to it being zero, as per the expression in (2b). The only left part of $M_{\mathrm{Cx\text{-}total}}$ is $M_{\mathrm{Cx\text{-}Rx}}$, which serves as the crucial component of the mapping indicator for motion trace detection, and it will be minutely analyzed for its magnitude and shifting trend.

When the Rx deviates from the central charging region of the Tx track, the values of $M_{\mathrm{Dx\_L\text{-}Tx}}$ and $M_{\mathrm{Dx\_R\text{-}Tx}}$ will change accordingly. One of these values will decrease while the other will increase within the preset effective detection and operation range. This shifting trend can be used to denote the Rx position regarding longitude misalignment direction and amplitude. Furthermore, the shifting of $M_{\mathrm{Cx\text{-}Rx}}$ occurs as Rx approaches the Cx coil during cyclic motion. This implies that the mapping indicator for detecting Rx motion trace can leverage this feature.

According to Fig. 3, the voltage on $L_{\mathrm{C}}$ and $L_{\mathrm{Dx\_L}}$ and $L_{\mathrm{Dx\_R}}$ can be obtained by

$$\dot{U}_C = j\omega L_{\mathrm{C}} \dot{I}_1 + j\omega I_{\mathrm{S}} M_{\mathrm{Cx-Rx}} \tag{3}$$

$$\dot{U}_{\mathrm{Dx\_L}} = j\omega L_{\mathrm{Dx\_L}} \dot{I}_2 + j\omega M_{\mathrm{D}} \dot{I}_2 + j\omega M_{\mathrm{Dx\_L-Rx}} \dot{I}_{\mathrm{S}} + j\omega M_{\mathrm{Dx\_L-Tx}} \dot{I}_{\mathrm{P}} \tag{4}$$

$$\dot{I}_{\mathrm{Dx\_R}} = j\omega L_{\mathrm{Dx\_R}} \dot{I}_2 + j\omega M_{\mathrm{D}} \dot{I}_2 + j\omega M_{\mathrm{Dx\_R-Rx}} \dot{I}_{\mathrm{S}} + j\omega M_{\mathrm{Dx\_R-Tx}} \dot{I}_{\mathrm{P}} \tag{5}$$

where $\dot{U}_C$ and $\dot{U}_{\mathrm{Dx\_}L}$ and $\dot{U}_{\mathrm{Dx\_}R}$ represent the vector form of $U_{\mathrm{C}}$ and $U_{\mathrm{Dx\_L}}$ and $U_{\mathrm{Dx\_R}}$, and $M_{\mathrm{D}}$ is the MI between the two Dx coils.

Based on the above derived equations as illustrated in (3)–(5), $M_{\mathrm{Dx\_L\text{-}P}}$ and $M_{\mathrm{Dx\_R\text{-}P}}$ and $M_{\mathrm{Cx\text{-}Rx}}$ can be calculated and obtained in the following equations:

$$M_{\mathrm{Cx-Rx}} = \frac{\dot{U}_C - j\omega L_{\mathrm{C}} \dot{I}_1}{j\omega} \tag{6}$$

$$M_{\mathrm{Dx\_L-Tx}} = \frac{\dot{U}_{\mathrm{Dx\_L}} - j\omega L_{\mathrm{Dx\_L}} \dot{I}_2 - j\omega M_{\mathrm{D}} \dot{I}_2 - j\omega M_{\mathrm{Dx\_L\text{-}S}} \dot{I}_{\mathrm{S}}}{j\omega \dot{I}_{\mathrm{P}}} \tag{7}$$

$$M_{\mathrm{Dx\_R-Tx}} = \frac{\dot{U}_{\mathrm{Dx\_R}} - j\omega L_{\mathrm{Dx\_R}} \dot{I}_2 - j\omega M_{\mathrm{D}} \dot{I}_2 - j\omega M_{\mathrm{Dx\_R\text{-}S}} \dot{I}_{\mathrm{S}}}{j\omega \dot{I}_{\mathrm{P}}}. \tag{8}$$

The expressions of mapping indicators for dual-objective Rx detection are given and investigated in Section IV with the above derived equation and its dynamic change mechanism.

### C. Basic WPT Characteristics

As Rx passes the preset trajectory points, the magnitude of $M_{\mathrm{Cx\text{-}Rx}}$ will change according to analysis, which is crucial for detecting the Rx motion trace but undesirable for the resonant *LCC-LCC* circuit. Therefore, alleviating the impact of $M_{\mathrm{Cx\text{-}Rx}}$ is necessary with the employment of the dual-side magnetic integration design.

The resonant characteristics of the proposed dual-side magnetic integration design depicted in Fig. 3 can be derived as [28]

$$\omega_0 L_{\mathrm{C}} = \frac{1}{\omega_0 C_{\mathrm{f1}}} \quad \omega_0 \left(L_{\mathrm{Dx\_R}} + L_{\mathrm{Dx\_L}} - 2M_{\mathrm{D}}\right) = \frac{1}{\omega_0 C_{\mathrm{f2}}} \tag{9}$$

$$\omega_0 (L_{\mathrm{P}} - L_{\mathrm{C}}) = \frac{1}{\omega_0 C_1}$$

$$\omega_0 \left[L_{\mathrm{S}} - (L_{\mathrm{Dx\_R}} + L_{\mathrm{Dx\_L}} - 2M_{\mathrm{D}})\right] = \frac{1}{\omega_0 C_2} \tag{10}$$

where $M_{\mathrm{D}}$ is the MI between Dx_L coil and Dx_R coil.

To assess the impact of dual-side magnetic integration design on WPT output performance, $I_{\mathrm{P}}$ need to be calculated, which can be derived as

$$\dot{I}_{\mathrm{P}} = \frac{j\omega {M_{\mathrm{CS}}}^3 \dot{I}_1 R - U_{\mathrm{in}} L_{\mathrm{C}}}{\omega^2 {L_C}^3 - j\omega M_{\mathrm{PS}} M_{\mathrm{CS}} R}. \tag{11}$$

The output power of the proposed *LCC-LCC* magnetic integration topology can be derived as

$$\dot{I}_1 = \frac{\dot{U}_1}{Z_{\mathrm{in}}} I_{\mathrm{P}} = \frac{U_{\mathrm{in}} - j\omega M_{\mathrm{Cx-Rx}} \dot{I}_{\mathrm{S}}}{j\omega L_{\mathrm{C}}} I_{\mathrm{R}} = \frac{j\omega M_{\mathrm{PS}} \dot{I}_{\mathrm{P}} + j\omega M_{\mathrm{Cx-Rx}} \dot{I}_1}{j\omega L_{\mathrm{C}}} \tag{12}$$

$$P_{\mathrm{out}} = \left[Re(\dot{I}_{\mathrm{R}})\right]^2 R \tag{13}$$

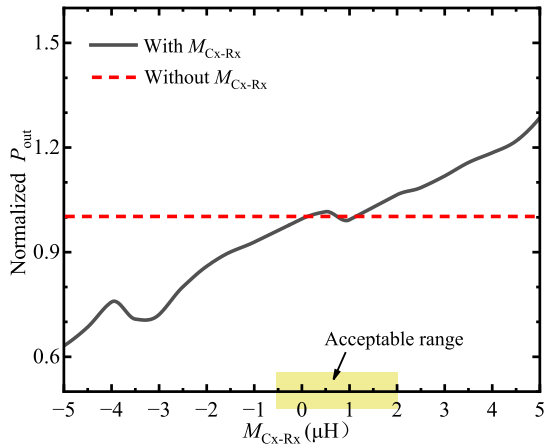


Fig. 5. Normalized output power ($P_{\text{out}}$) as a function of $M_{\text{Cx-Rx}}$.

where $\dot{U}_1$ is the output voltage of the high-frequency inverter, and $\dot{I}_R$ represents the current flowing through the load.

The mathematical expression for $P_{\text{out}}$ is complex and is not addressed in this part. To clearly exhibit the impact of $M_{\text{Cx-Rx}}$, a simulation for WPT output performance comparison is performed in Fig. 5, in which the component parameters are appropriately selected to evaluate the influence.

Fig. 5 shows that the normalized output power experiences rapid fluctuations when $M_{\text{Cx-Rx}}$ exceeds 2 $\mu$H or drops below $-1$ $\mu$H. When it reaches 5 $\mu$H, the output power undergoes a significant change, which severely affects the system's output stability. Therefore, it is recommended to maintain $M_{\text{Cx-Rx}}$ fluctuations within an acceptable range as the Rx coil approaches the Cx coil, with the peak value of $|M_{\text{Cx-Rx}}|$ not exceeding 1 $\mu$H and power fluctuations limited to 5%.

By combining (9) and (10), the input impedance can be derived as

$$Z_{\text{in}} = \frac{{\omega_0}^2 {L_{\text{C}}}^4}{R_{\text{L}} M_{\text{PS}}^3} - 2\frac{j\omega_0 L_{\text{C}} M_{\text{CS}}^2}{M_{\text{PS}}}. \tag{14}$$

The presence of the imaginary part in accordance with (14) is inevitable as the Rx passes the Cx coil. This underscores the importance of setting its magnitude reasonably. The resonant frequency of the system is chosen as 85 kHz, assuming that the magnitude of the related self-inductance is ten to the power of negative three, although this is not possible for practical application. It becomes evident that the imaginary part of the input impedance is ten to the power of negative six, particularly when $M_{\text{PS}}$ is larger than $M_{\text{Cx-Rx}}$. As a result, the impact of Rx passing the preset points next to the Cx coil on the proposed system resonant characteristics is almost negligible, thereby without affecting WPT performance.

## III. Integrated Coils' Design for Dynamic Rx Positioning

Thoughtful integrated coil design is crucial for enhancing dynamic detection accuracy and ensuring reasonable boundaries

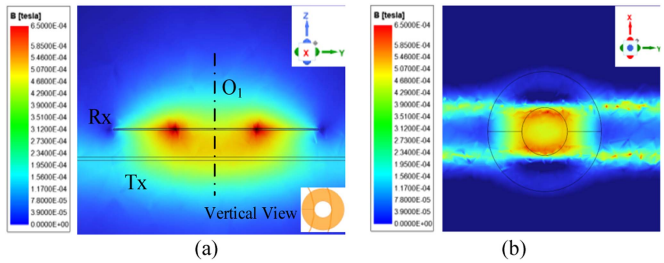


Fig. 6. Simulation for magnetic field distribution. (a)YZ plane ($x = 0$ mm). (b) XY plane ($z = 20$ mm).

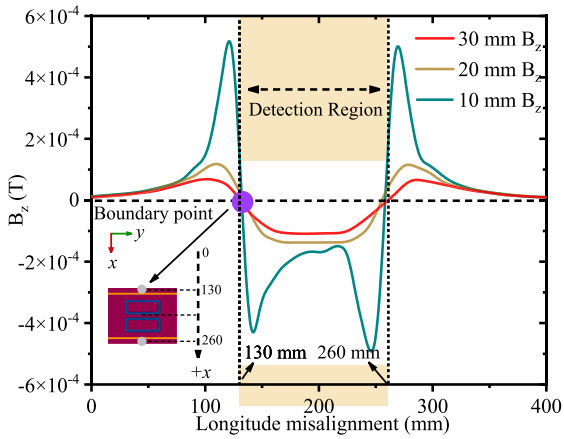


Fig. 7. Magnetic flux density in the $z$-direction at different heights above the Tx track.

for ceasing operation of the automatic vehicles in uninventable malfunction condition. In this context, several key parameters of the Dx coils and the shifting trend of $M_{\text{Cx-Rx}}$ are the crucial optimizing and study emphasis in the following analyses.

The height at which the Dx coils is positioned is crucial for detecting longitude misalignment direction and amplitude since the coverage of the magnetic flux penetration is nonlinearly decreased with the increasing height. Physical meaning, the value of $M_{\text{Dx\_L-Tx}}$ and $M_{\text{Dx\_R-Tx}}$ varies significantly at different heights above the Tx track, and undesired values may pose a challenge to accurate positioning. Fig. 6 presents the magnetic field shaping effects produced by the Tx coil at the heights of 20 mm above the Tx track, denoting that the magnetic flux density is mainly concentrated in the $z$-direction. This means that a $B_z$ curve with relatively smooth characteristics and a distinct transition boundary is conducive to Rx misalignment detection. Fig. 7 shows the magnetic flux density in the Z direction at various heights of the long-track Tx coil. It is evident that $B_z$ exhibits significantly more variation at 10 mm above the Tx coil compared to heights of 20 mm and 30 mm. Therefore, to obtain smoother $M_{\text{Dx\_L-Tx}}$ and $M_{\text{Dx\_R-Tx}}$ curves, the transfer distance $h$ and the distance between Dx coils and Tx coil $h_{\text{DT}}$ are set to be 35 mm and 22 mm, respectively.

The zero-crossing points of these sweeping curves are marked as boundary points in Figs. 7 and 8. This signifies that the position detection accuracy of the Dx coil is severely affected when

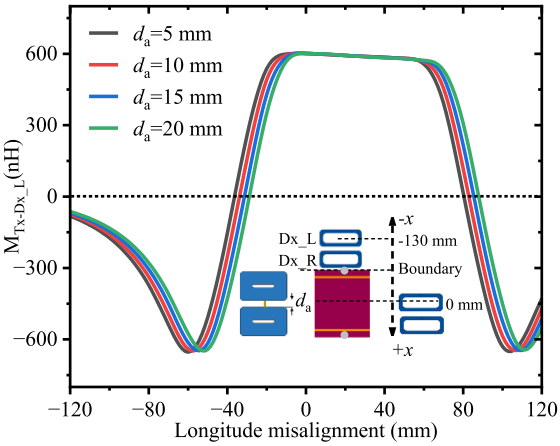


Fig. 8. $M_{\mathrm{Dx\_L\text{-}Tx}}$ versus longitude misalignment with different $d_a$ values.

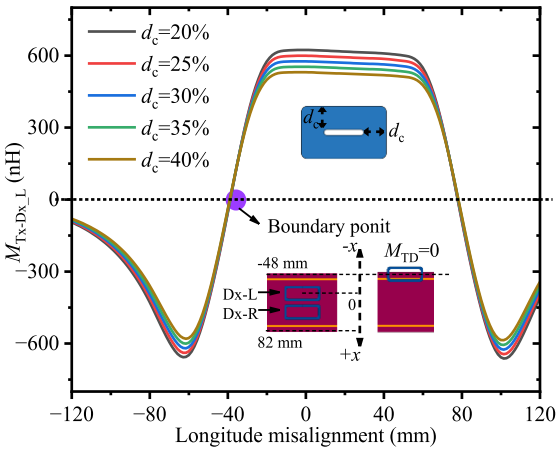


Fig. 9. $M_{\mathrm{Dx\_L\text{-}Tx}}$ versus longitude misalignment with different $d_c$ values.

Rx deviates too far from the energizing Tx track. Therefore, it is advisable to set the boundary threshold reasonably during the actual operation process, thereby ceasing the automatic vehicles in time.

A large gap between the two Dx coils can potentially cause abrupt changes in the parameters $M_{\mathrm{Dx\_L\text{-}Tx}}$ and $M_{\mathrm{Dx\text{-}R\text{-}Tx}}$ even for slight misalignments, consequently resulting in significant positioning errors in situations where no misalignment is present. Fig. 8 portrays the change in $M_{\mathrm{Dx\_L\text{-}Tx}}$ versus longitude misalignment, for different inner spacing distances ($d_a$) between the two Dx coils, indicating that as the gap distance increases, the curve holds a narrower stable range. To provide a clear boundary operation point and facilitate the compactness while mitigating the adverse proximity effects between two Dx coils, a value of 10 mm is selected for $d_a$.

The inner coverage and width ($d_c$) of the Dx coils is a key parameter that affects its coupling intensity with the Tx coil, indicating that the length and effectiveness of the magnetic flux pipe concentrated on the central coupling area are governed by the coverage of the midsection. It can be observed from Fig. 9 that as $d_c$ increases, the zero-crossing point does not shift, and the stable range of the curve sees a steady trend with different

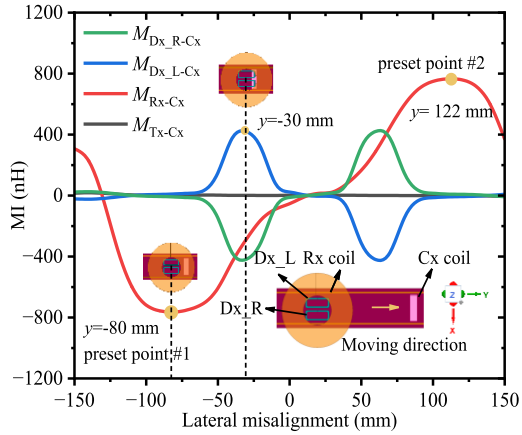


Fig. 10. MIs between the Dx and Tx coils, the Cx and Rx coils, and the Tx and Cx coils versus the lateral misalignment along the Tx track.

$d_c$ values. As a result, a $d_c$ value of 35% is selected to ensure the amplitude of $M_{\mathrm{Dx\text{-}Tx}}$ is detectable for deriving its corresponding mapping indicator.

Having a clearly shifted curve of $M_{\mathrm{Cx\text{-}Rx}}$ within an acceptable range is crucial for Rx motion trace detection and efficacy dynamic charging, as demonstrated in Fig. 5. Fig. 10 depicts the MIs for different coil combinations. It can be found that the absolute peak value of $M_{\mathrm{Cx\text{-}Rx}}$ is almost 0.8 $\mu$H, which is large enough to be utilized for making the related mapping indicator. It also implies that two trajectory points could be set at the front and rear end of the Cx coil at which the peak value is positioned, by which the mapping indicator for detecting motion trace can utilize the two preset points to count the motion cycles of automatic vehicles with recognizable and precise counting marks.

## IV. Dual-Objective Rx Detection Strategy Based on the Mapping Deviations

### A. Detection Mapping Indicators and Rx Rotation Analysis

Based on the dual objective Rx detection principle, two mapping indicators are proposed to detect the Rx deviation, misalignment amplitude, and timings for passing preset trajectory points. These indicators leverage the characteristics of $M_{\mathrm{Dx\_L\text{-}Tx}}$, $M_{\mathrm{Dx\text{-}R\text{-}Tx}}$, and $M_{\mathrm{Cx\text{-}Rx}}$, and the Rx detection strategy and proceeds are comprehensively described in conjunction with the derived mapping indicators in the following investigation.

The values of $M_{\mathrm{Dx\_L\text{-}Tx}}$ and $M_{\mathrm{Dx\text{-}R\text{-}Tx}}$ will exhibit opposite trends, with one increasing and the other decreasing, whether in downward or upward deviation direction. In this way, $O^*$ is defined as the first mapping indicator with the exploitation of this characteristic to realize offset direction and amplitude detection, and its expression is derived as

$$O^* = \frac{M_{\mathrm{Dx\_L-Tx}}}{M_{\mathrm{Dx\_R-Tx}}}. \tag{15}$$

If $O^* > 1$, with the assumption that there is a threshold point for ceasing operation, the $M_{\mathrm{Dx\_L\text{-}Tx}}$ coil has a relatively larger

amplitude than $M_{\mathrm{Dx\_R\text{-}Tx}}$, implying that the Dx_R coil deviates along the Tx track in a downward direction. Conversely, if $O^*<1$, the deviation direction would be upward. As for the specific function, the $O^*$ is being utilized to detect the deviation direction and misalignment amplitude of the Rx to avoid unwanted power transfer valleys and manufacturing efficiency.

When the Rx is far from the Cx coil, denoting $M_{\mathrm{Cx\text{-}Rx}}$ is zero, the voltage on $L_{\mathrm{C}}$ can be expressed as

$$\dot{U}_{\mathrm{C}}^{(\mathrm{S})} = j\omega L_{\mathrm{C}}\dot{I}_1 \tag{16}$$

where the superscript (S) means the preset values for the controller.

$M_{\mathrm{Cx\text{-}Rx}}$ is inevitable and its impact on WPT input and output performance is negligible based on the presented analysis in the last section. Thus, the second mapping indicator for detecting the motion trace of automatic vehicles can be deduced as

$$T^* == \frac{U_{\mathrm{C}}^{(\mathrm{R})} - U_{\mathrm{C}}^{(\mathrm{S})}}{\omega I_{\mathrm{S}}} \tag{17}$$

where the superscript (R) means the real-time calculated values for the controller.

Two preset trajectory points are established, corresponding to the positive and negative peak values of $M_{\mathrm{Cx\text{-}Rx}}$ as shown in Fig. 10. During practical operation, these values serve as reference points for comparison, where real-time calculated values of $T^*$ are compared with preset thresholds value. This process results in the generation of two trigger pulses by the system controller within a single motion cycle, one positive and the other negative, and thereby the motion cycle numbers will be counted to supervise the yearly maintenance deadline.

The preset threshold for motion trace detection may not perfectly align with practical operation, potentially leading to missed trigger pulses. Automatic vehicles typically have motion cycles that span tens of seconds, allowing the system to identify motion cycle numbers despite missing trigger pulses thanks to the significant time gap between contiguous cycles.

The angular offset is inevitable due to unintentional collision or transient navigation errors. As a result, determining how the angular offset affects detection accuracy is crucial. The observation reveals a steady decrease in the length of the stable range of $M_{\mathrm{Dx\_L\text{-}Tx}}$ as the angular misalignment increases as shown in Fig. 11. This suggests that large angular misalignment is not advantageous for Rx detection, as the values of $M_{\mathrm{Dx\_L\text{-}Tx}}$ or $M_{\mathrm{Dx\text{-}R\text{-}Tx}}$ decreases rapidly, perhaps more quickly reaching the boundary point at which the system will drive to ceasing operation. Consequently, making a judicious selection of boundary points, taking into account the maximum offset angle and the width of the charging region, is critical. This aspect will be discussed and analyzed in detail in Section V.

### B. Rx Detection Proceeds

The proposed dual-objective Rx detection strategy proceeds are presented in Fig. 12, in which the deviation direction, longitude misalignment amplitude, and motion trace are detected by leveraging the shifting trend of the specific MIs.

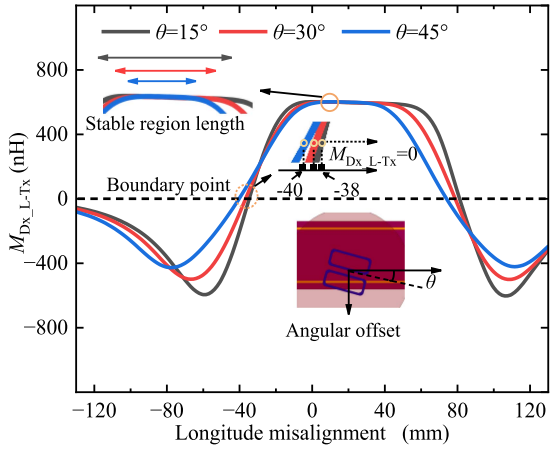


Fig. 11. $M_{\mathrm{Dx\_L\text{-}Tx}}$ versus longitude misalignment with various angular offset values.

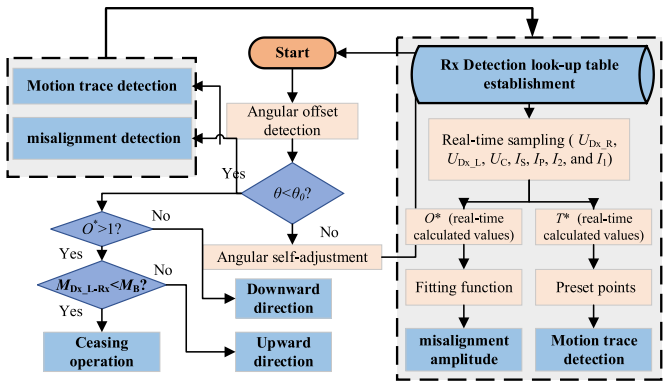


Fig. 12. Flowchart of the proposed dual-objective Rx detection strategy.

In the proposed detection flowchart for the Rx, conditions of large angular offsets are excluded due to the scaled-down model's relatively narrow track width in the experiment setup, which is not conducive to accurate Rx detection at such angles. In this way, $\theta_0$ is set for large angular misalignment judgment, by which the angular self-adjustment is conducted after the judgment. The detection processes for deviation direction, misalignment amplitude, and motion trace are proceeded within reasonable angular offset. The establishment of $M_{\mathrm{B}}$ is necessitated by the peculiar mathematical expression for $O^*$. Specifically, as the system experiences downward offset, the value of $O^*$ increases beyond 1. However, once it surpasses the designated boundary point, the value of $O^*$ begins to decrease again. This creates a scenario where two different offset distances correspond to the same value of $O^*$, potentially leading to significant errors in positioning accuracy if not properly addressed.

The process begins with the implementation of angular offset judgment. This is followed by real-time fast Fourier transform (FFT) computation in the microcontroller unit, insertion of the $O^*$ value into the established fitting function, and comparison with values appointed by preset trajectory points. These steps collectively facilitate the detection of deviation direction, misalignment amplitude, and the number of motion cycles as the Rx operations cyclically along the Tx track.

TABLE III
PARAMETER VALUES OF THE DEVELOPED EXPERIMENTAL PROTOTYPE

| Parameter | Value | Parameter | Value |
|---|---|---|---|
| $L_C$ | 12.1 $\mu$H | $C_2$ | 35 nF |
| $C_1$ | 637.4 nF | $C_{f2}$ | 292.1 nF |
| $C_{f1}$ | 289.7 nF | $L_{D\_L}$ | 8.5 $\mu$H |
| $L_P$ | 23.5 $\mu$H | $L_{D\_R}$ | 8.6 $\mu$H |
| $L_S$ | 118.5 $\mu$H | $C_B$ | 539 nF |

### C. Positioning Accuracy Analysis Given Dynamic Operation

To verify the dynamic positioning capabilities of the proposed dual-objective RPD method, the communications between different sectors and the motion speed of the automatic vehicles in the proposed long-track DWPT system are required for analysis. The time needed for a single point position information obtainment can be calculated as [28]

$$t = 2t_d + t_m + t_c + t_p \tag{18}$$

where $t_d$ represents the delay time for high-frequency ADC sampling and filtering, $t_m$ represents the interactive time for high-frequency signal processing and message passing between the controller and sampling components, $t_c$ signifies the time for logical operation regarding the multichannel FFT analysis toward the mapping indicators' calculation, and $t_p$ denotes the time for comparison between stored values and real-time calculated values.

In the actual process of dynamic misalignment and motion trace detection, the accessible operation time for the automatic vehicles is limited by the angular offset because of the fixed track width. Each system component, from high-frequency sampling circuits to FFT computation software and position information logic flow, requires a certain amount of time during which the vehicle continues its journey. Therefore, to achieve accurate position detection, especially at higher speeds such as 1 m/s, it is crucial to ensure that the DWPT system completes the current single-point position detection process before reaching the next preset sampling interval.

## V. EXPERIMENTAL VERIFICATION AND PERFORMANCE COMPARISON

### A. Experimental Prototype Setup

A scaled-down long-track DWPT experimental prototype, energized with 85 kHz frequency, is established to assess the effectiveness and rationality of the proposed dual-objective Rx detection method and magnetic integration design. The Cx coils are implemented slightly above the Tx track, as presented in Fig. 13(a). Two Dx coils are placed parallel with the Rx coil to form the position detection assembly which is installed on the vehicle's chassis as illustrated in Fig. 13(b) and (c). An infrared tracking vehicle is utilized to demonstrate the feasibility and efficacy of the proposed RPD method, in which the high-frequency voltage and current transformers are installed to measure the Rx side mapping indicators' elements. The long-track DWPT system parameters can be found in Table III. GPCT03Z pulse-type high-frequency current and voltage transformers, along with a

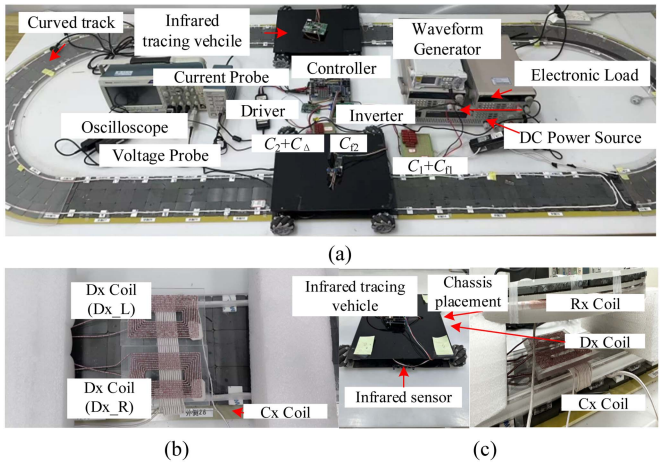


Fig. 13. Long-track DWPT experimental prototype overall view and close-up depictions. (a) Overall view of the long-track DWPT experimental prototype. (b) Integrated coils' design. (c) Infrared tracing vehicle equipped with Rx detection assembly and high-frequency current and voltage transformers.

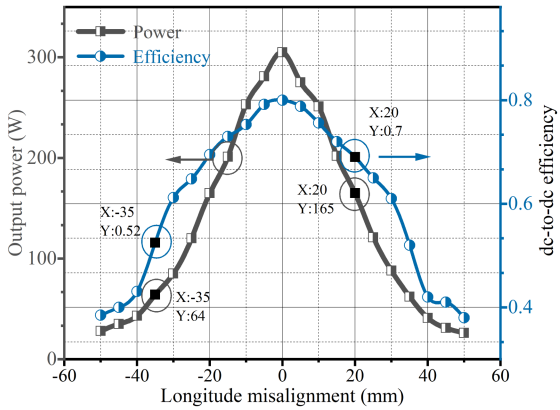


Fig. 14. Output power and DC–DC efficiency of the long-track DWPT prototype as the offset varies from −60 to 60 mm with two Rxs' implementation.

four-channel ADC sampling integrated circuit embedded into the controller, are utilized to measure the objective parameters. STM32F103 is selected for the controller to conduct mapping indicators computation and position determination by sending the calculated value into the piecewise fitting functions. Counting the vehicle's motion cycles is managed by setting two thresholds for $T^*$. The system performs a count whenever the measured absolute values satisfy the condition of being greater than these thresholds. The output power and dc–dc efficiency of the long-track DWPT system decline sharply when the misalignment exceeds 30 mm, as is shown in Fig. 14. This highlights the need for Rx detection for automatic vehicles in industrial settings. The presented efficiency calculation method includes the transfer efficiency of the converters, showing acceptable compared to the method presented in [18].

The inevitable power fluctuations as analyzed in Section II need to be seriously addressed under this integration design concept. Figs. 15 and 16 present the input and output shifting trend of this DWPT system as the Rx approaches and strays from the Cx coil. From Fig. 15, the zero-phase angle is essentially

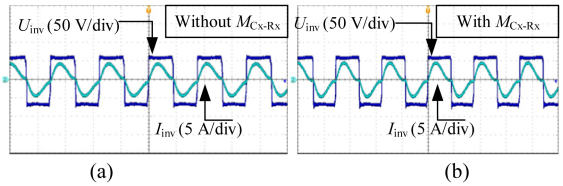


Fig. 15. Experimental waveforms of the input inverter. (a) Without $M_{\text{Cx-Rx}}$. (b) With $M_{\text{Cx-Rx}}$.

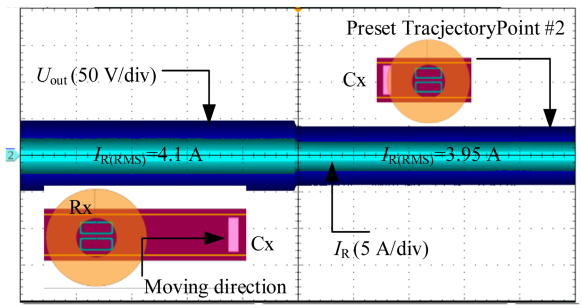


Fig. 16. Experimental waveforms of the output current and voltage when Rx passes the preset trajectory points ($R_L$=15 Ω).

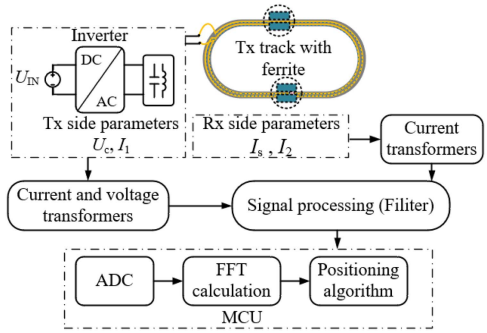


Fig. 17. Practical positioning flow in the hardware section.

achieved, demonstrating the effectiveness of this topology. The variation in output power is constrained within a range of ±5% when the maximum negative and positive amplitudes of $M_{\text{Cx-Rx}}$ are reached. The notable power fluctuations depicted in Fig. 16 are due to the change of $M_{\text{Cx-Rx}}$ and are partially affected by the rated power transmission limit and attenuation factors of the voltage and current probe, leading to a degree of visual discrepancy. Fig. 17 presents the practical procedure of the proposed dual-objective RPD method, in which the computation elements of the mapping indicators are measured by the transformers.

### *B. Operation Speed Analysis and Positioning Look-Up Fitting Function Establishment*

As discussed in the previous section, the magnitude of the angular offset influences the selection of boundary points. In this experiment, considering the optimized structural parameters of the Dx coils and the limited track width in this downsized experimental model, the location coordinates of the two specified boundary points on both sides are −42.50 mm and 42.50 mm,

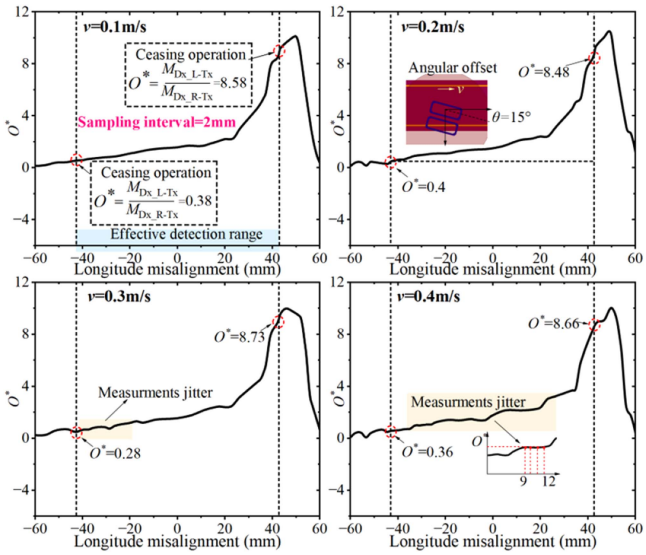


Fig. 18. Measurements of $O^*$ as the offset varies from −60 to 60 mm with different operational speeds and fixed angular offset ($\theta = 15°$, sampling interval = 2 mm).

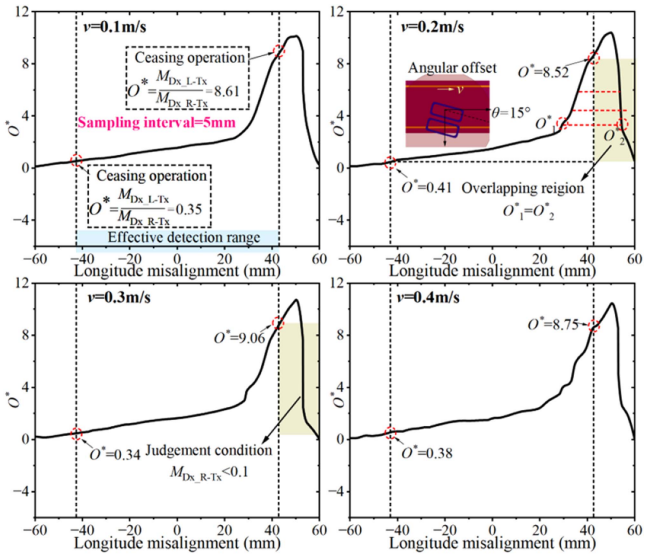


Fig. 19. Measurements of $O^*$ as the offset varies from −60 to 60 mm with different operational speeds and fixed angular offset ($\theta = 15°$, sampling interval = 5 mm).

respectively. This is based on the angle impact analysis from simulations and data obtained from experimental measurements as depicted in Figs. 11 and 18. Correspondingly, the values for $O^*$ are set at "0.40" and "8.50" for these preset boundary points for ceasing operation judgment conditions.

Dynamic Rx detection requires robust and fast monitoring data transmission capabilities. To demonstrate how the operational speed of the infrared tracing vehicles impacts the accuracy of the real-time measurement $O^*$ values, two sets of experiments with different sampling intervals are conducted. Figs. 18 and 19 present the measurements of $O^*$ as the longitude offset varies from −60 to 60 mm with different running speeds and fixed angular offset. Fig. 17 clearly shows that as the speed increases,

the fitting curve of the measured $O^*$ values exhibits noticeable jitter. Particularly at a speed of 0.4 m/s, the degree of jitter intensifies, leading to data overlap. This results in a single $O^*$ value corresponding to two different longitude offsets within the effective positioning region, which severely undermines positioning accuracy. When the sampling interval is increased to 5 mm, Fig. 18 indicates that although there are still some data fluctuations at 0.4 m/s, the fitting curve derived from the 65 collected points along the line inclined at 15° does not exhibit the same level of disarray.

For a complete Rx detection process in this experiment, $t_{\mathrm{d}}$ is typically set to 120 ns which accounts for five times the ADC circuit's time constant and includes the transformer capture delay. A typical value of $t_{\mathrm{m}}$ is 5 ms for the objective four-channel packetization and transmission. A typical value of $t_{\mathrm{p}}$ is 2.5 ms for single point positioning with an assumption that there is only one offset direction in a complete RPD process, with the controller working at 1 MHz crystal frequency. The two stages of validation require 18 and 33 points, respectively, and the long-track DWPT system necessitates 200 ms to achieve a stable output. Thus, the total time needed to complete these two RPD processes can be estimated at 0.26 s and 0.29 s, respectively. The Rx traverses through the sampling intervals of 2 mm and 5 mm in 5 ms and 12.5 ms, respectively, with a single position detection cycle taking approximately 7.6 ms. This timing explains why data jitter becomes more pronounced when the sampling interval is reduced to 2 mm, as the vehicle has moved to the next interval before the current positioning process is completed.

Consequently, this experiment will employ a sampling interval of 5 mm and establish a set of piecewise fitting functions between adjacent points. By inputting the real-time measured $O^*$ values into these established piecewise fitting curves, the offset direction and amplitude can be determined. Furthermore, it is evident that due to the specific definition of $O^*$, there is a recurring phenomenon of $O^*$ values as the downward offset distance increases. This is marked in the yellow region in Fig. 19. As a result, "$M_{\mathrm{Dx\_R\text{-}Tx}}$<0.10" must be implemented as an additional criterion for judgment. Even if the $O^*$ value features the same amplitude as its counter in the effective recognition area, the vehicle will still be deemed to have surpassed the operational boundary of the long-track DWPT system. This supplementary condition illustrated in Fig. 12 serves to avert erroneous positioning conditions.

Based on the 18 gathered points measured along the longitude direction and predetermined effective detection range, the linear piecewise fitting function for misalignment detection can be deduced as

$$D_i = k_i O^*_{(i)} + b_i (i = 1, 2, 3.., 18) \tag{19a}$$

$$\begin{cases} k_i = \dfrac{D_{i+1} - D_i}{O^*_{(i+1)} - O^*_{(i)}} \\ b_i = D_i - k_i O^*_{(i)} \end{cases} (i = 1, 2, 3.., 18) \tag{19b}$$

where $O_i{}^*$ represents the measured value of the $i$th $O^*$, $k$ denotes the slope of the fitting function, $D_{\mathrm{i}}$ indicates the offset distance corresponding to the $i$th $O^*$, and $b_i$ is the constant term of the fitting function.

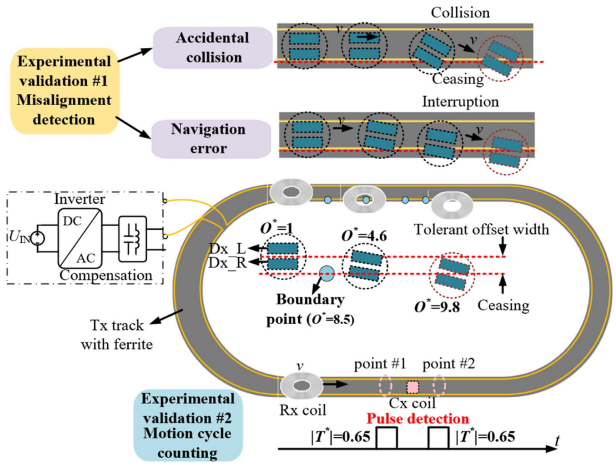


Fig. 20. Experimental validation flow of the proposed RPD method.

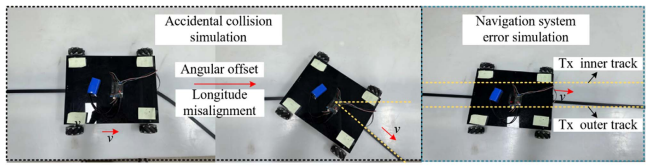


Fig. 21. Simulation of practical operational malfunctions with infrared tracing vehicle and black dotted trajectories. (a) Accidental collision simulation. (b) Navigation system error simulation.

By employing the established fitting function, the misalignment amplitude and direction can be detected. This is achieved by inputting the real-time measurements of the $O^*$ values into the preset linear piecewise fitting function, thereby facilitating precise and timely detection.

The look-up positioning fitting function expression can be derived as

$$\begin{cases} D_1 = k_1 O^*_{(1)} + b_1 (0.40, 0.46] \\ D_2 = k_2 O^*_{(2)} + b_2 (0.46, 0.50] \\ \cdots\cdots\cdots \\ D_{35} = k_{35} O^*_{(35)} + b_{35} (7.92, 8.50) \end{cases} . \tag{20}$$

Note that the measured point for real-time positioning is obtained in manual work without angular offset.

### C. Experimental Validation Results of the Dual-Objective RPD Method

Two prevalent erroneous scenarios in industrial operations of automatic vehicles are chosen to validate the misalignment detection capability of the proposed Rx positioning strategy, as shown in Fig. 20. Preset trajectory points near the Cx coil are set for the motion trace detection. The infrared tracing vehicle, along with the Rx detection setup, operates at a speed of 0.3 m/s. During the validation phase, two kinds of black-dotted trajectories simulate the accidental collision and navigation system errors as depicted in Fig. 21.

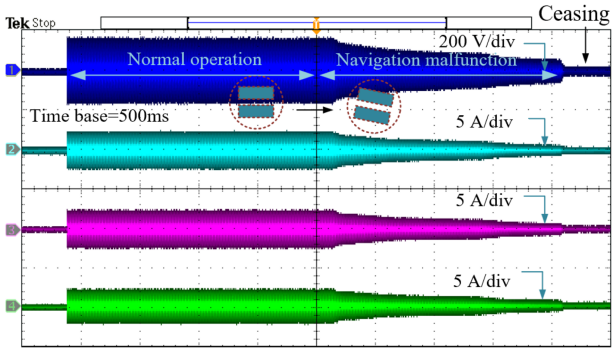


Fig. 22. Experimental waveforms of $U_C$, $I_1$, $I_S$, and $I_2$ when the Rx deviates in a downward direction at a constant angle of 20°.

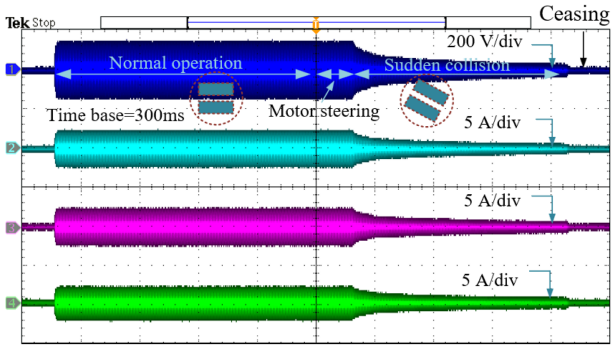


Fig. 23. Experimental waveforms of $U_C$, $I_1$, $I_S$, and $I_2$ when the Rx deviates in a downward direction at a sudden angular offset of 45°.

Figs. 22 and 23 show the variations in the $O^*$ related calculation parameters under two distinct offset scenarios of the vehicle. The waveform simulating a navigation failure shows a gradual change trend ($\theta = 20°$), indicative of the vehicle's slow deviation. Conversely, the waveform simulating an unexpected collision reveals a rapid change in trend following an angular offset ($\theta = 45°$), suggesting a more abrupt displacement.

This underscores the importance of setting appropriate boundary points in accordance with the layout of the long-track DWPT system. Properly established boundaries prevent the sudden cessation of the vehicle's operation due to unexpected angular errors, which could lead to extensive operational paralysis. Note that the continuous waveforms depicted in Figs. 22 and 23 were obtained from an oscilloscope set at 2048 sampling length with time bases of 500 ms and 300 ms, respectively. These settings were selected to effectively demonstrate the variation of parameters under angular and longitude offset changes and to illustrate the steps involved in FFT analysis. However, for the actual position detection, the sampling precision of the voltage, and current transformers on the Tx and Rx side are controlled at 5 mm. This level of precision is maintained to prevent disarray and confusion in the measurement data, ensuring accurate and reliable positioning.

Fig. 24 presents the waveform regarding motion trace detection, in which positive and negative trigger pulses occur in cyclic motion. From Fig. 10, the two preset trajectory points are located at the positive and negative peak values, respectively, which are

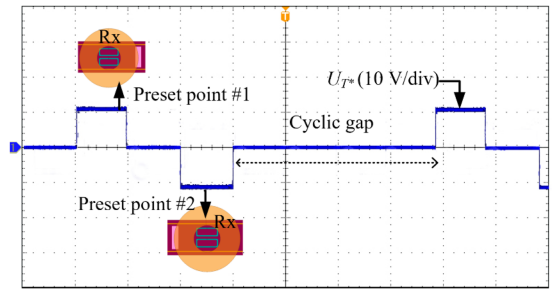


Fig. 24. Experimental trigger pulses when the Rx passes two preset trajectory points along the Tx track.

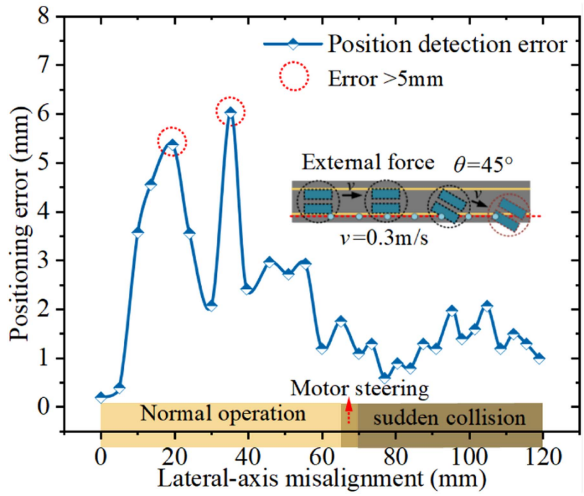


Fig. 25. Rx position detection results for the simulation of accidental collision when the infrared tracing vehicle operation at 0.3 m/s.

$\pm 0.8$ $\mu$H. To effectively capture the motion cycle numbers, $T^*$ is set to be $\pm 0.65$ $\mu$H as an experimental threshold. The positive and negative trigger pulses are set in case of multiple triggers in a single motion cycle.

From the analysis, the positioning errors shown in Figs. 25 and 26 can be explained as the time difference between the circuit and the vehicle's motion speed. Notably, as the speed increases, the positioning errors are observed to enlarge correspondingly.

Additionally, it can be seen from both figures that significant positioning errors occur even when no offset is present. This is attributed to the vehicle being in an MI stable region where the variation of $O^*$ is not as obvious compared to when a misalignment occurs. Consequently, the calculated $O^*$ might be incorrectly placed into the wrong positioning piecewise function, leading to substantial errors.

Table IV reviews and compares a variety of Rx detection methods. Magnetoresistive sensor arrays are arranged to detect the Rx's misalignment [13]. The required sensors' numbers are high, which leads to significant costs for their configuration. Vehicle-side pulse detection method is proposed in [22], but the mounted GPS module is needed for the start of the positioning process. For the methods in [24], [25], [27], and [28], auxiliary positioning coils are employed. Phase-locked loop chips are implemented to detect multiple phase differences [24]. Three

TABLE IV
COMPARISONS WITH SIMILAR RX DETECTION METHODS

| Methods | Magnetic integration | Detection objective | Motion speed consideration | Positioning principle | Overall cost |
|---|---|---|---|---|---|
| **[13]** | No | Misalignment detection | No | Magnetic field strength sensing | ★★★★★ (magnetoresistive sensor arrays) |
| **[22]** | No | Timely road-side coil activation | Yes | Vehicle-side voltage pulse | ★★★★ (GPS and activation circuits) |
| **[24]** | No | Relative position detection of the Rx and Tx coils | No | Square waves' phase comparison | ★★★ (2 auxiliary circuits; Multiplexers and phase-locked loop chips) |
| **[25]** | No | Relative position detection of the Rx and Tx coils | Yes | Region partition algorithm | ★★★ (3 parallel switch-controlled circuits and 1 master control switch) |
| **[27]** | No | Misalignment detection | No | Coupling coefficient calibrations | ★★★ (1 extra inverter) |
| **[28]** | No | Misalignment detection | No | Induced voltage processing | ★★★ (2 auxiliary energizing circuits with signal processing loops) |
| **[29]** | Yes (Single side) | Misalignment detection | No | 4 positioning mapping indicators | ★★ (1 driver circuit with controller) |
| This article | Yes (Dual side) | Misalignment and motion trace detection | Yes | 2 positioning mapping indicators | ★★ (No extra sensors, extra energizing circuits, and control switches) |

The number of ★ represents the cost level.

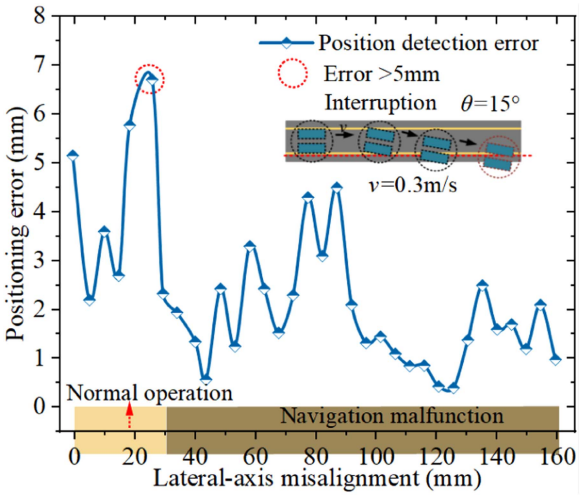


Fig. 26. Rx position detection results for the simulation of navigation system malfunction when the infrared tracing vehicle operation at 0.3 m/s.

parallel switched-control circuits with a master control stage are set in the Rx detection process in [25]. Two inverters are required for powering the main transformer and the auxiliary network in research work in [27]. Two extra energizing circuits independent from the main power transfer network are installed in the research presented in [28].

Compared to [26], the sampling interval selection for alleviating the impact of the vehicle's speed is conducted in this article, and the boundary point determination is also discussed under dynamic operation. Compared to [28], which also employs two types of auxiliary coils, this article integrates two auxiliary coils into the bridge inductors of the *LCC-LCC* circuit, achieving more cost-effective Rx position identification. Additionally, it eliminates the need for extra excitation circuits and realizes dual-objective positioning aims, which facilitates functionality and practicality in real industrial settings. Unlike the unilateral magnetic integration positioning method used in [29], which introduces four positioning mapping indicators for four paths' detection along the diagonal line in the plane of the Tx coil, this article employs just two positioning mapping indicators to accomplish the detection process. This reduces computational complexity and also takes into account the impact of speed on positioning accuracy. A possible drawback of this method proposed in this article is that the operational speed of the automatic vehicles needs to be fixed during the practical Rx detection process.

## VI. CONCLUSION

This article proposes a dual-objective Rx detection method, employing magnetically integrated coils for detecting the Rx's longitude misalignment and motion trace in the long-track DWPT systems, which holds the potential for applying to other DWPT systems with certain adaptations. This method effectively identifies Rx positions under angular misalignment and dynamic conditions, within the system's effective detection range. Compared to prior coil positioning methods, the proposed Rx detection strategy holds a dual-objective Rx detection aim with cost-effective auxiliary coils' integration assembly, dynamic positioning without affecting WPT performance, and a simplified position detection procedure based on defined mapping relationships. A scaled-down long-track DWPT

experimental prototype is established to validate the dynamic positioning capabilities of the proposed RPD method. The experimental results indicate that the measurements jitter can be alleviated by appropriately selecting the sampling interval and thereby avoiding large positioning errors. The positioning errors under the two tested malfunction conditions are found to be less than $\pm 8$ mm.

## REFERENCES


[1] X. Li, C. Wang, H. Wang, X. Dai, Y. Sun, and A. P. Hu, "A robust wireless power transfer system with self-alignment capability and controllable output current for automatic-guided vehicles," *IEEE Trans. Power Electron.*, vol. 38, no. 10, pp. 11898–11906, Oct. 2023.

[2] C. Zhu et al., "Analysis and design of cost-effective WPT systems with dual independently regulatable outputs for automatic guided vehicles," *IEEE Trans. Power Electron.*, vol. 36, no. 6, pp. 6183–6187, Jun. 2021.

[3] S. J. Huang, T. S. Lee, W. H. Li, and R. Y. Chen, "Modular on-road AGV wireless charging systems via interoperable power adjustment," *IEEE Trans. Ind. Electron.*, vol. 66, no. 8, pp. 5918–5928, Aug. 2019.

[4] C. C. Mi, G. Buja, Y. C. Su, and C. T. Rim, "Modern advances in wireless power transfer systems for roadway powered electric vehicles," *IEEE Trans. Ind. Electron.*, vol. 63, no. 10, pp. 6533–6545, Oct. 2016.

[5] H. Feng, R. Tavakoli, O. C. Onar, and Z. Pantic, "Advances in high-power wireless charging systems: Overview and design considerations," *IEEE Trans. Power Electron.*, vol. 6, no. 3, pp. 886–919, Sep. 2020.

[6] L. Tan, Y. Yu, J. Wang, R. Wang, and C. Li, "Research on grid positioning strategy of coupling mechanism in wireless charging system with offset angle variable," *IEEE Trans. Power Electron.*, vol. 38, no. 5, pp. 6670–6681, May 2023.

[7] A. C. Bagchi, A. Kamineni, R. A. Zane, and R. Carlson, "Review and comparative analysis of topologies and control methods in dynamic wireless charging of electric vehicles," *IEEE J. Emerg. Sel. Topics Power Electron.*, vol. 9, no. 4, pp. 4947–4962, Aug. 2021.

[8] E. Lee, M. Kim, S. Kang, and S. Han, "Segmented IPT coil design for continuous multiple charging of an electrified monorail system," *IEEE Trans. Power Electron.*, vol. 37, no. 3, pp. 3636–3649, Mar. 2022.

[9] S. Choi, J. Huh, W. Lee, S. Lee, and C. Rim, "New cross-segmented power supply rails for roadway-powered electric vehicles," *IEEE Trans. Power Electron.*, vol. 28, no. 12, pp. 5832–5841, Dec. 2013.

[10] M. Budhia, G. A. Covic, and J. T. Boys, "Design and optimization of circular magnetic structures for lumped inductive power transfer systems," *IEEE Trans. Power Electron.*, vol. 26, no. 11, pp. 3096–3108, Nov. 2011.

[11] W. Chen, F. Lin, and G. A. Covic, "A modified DDQ track for interoperable EV dynamic charging," *IEEE Trans. Power Electron.*, vol. 38, no. 11, pp. 1738–11750, Oct. 2023.

[12] A. Babu and B. George, "Sensor system to aid the vehicle alignment for inductive EV chargers," *IEEE Trans. Ind. Electron.*, vol. 66, no. 9, pp. 7338–7346, Sep. 2019.

[13] J. T. Vaheeda and B. George, "TMR sensor-based detection of EVs in semi-dynamic traffic for optimal charging," *IEEE Trans. Intell. Transp. Syst.*, vol. 23, no. 8, pp. 13721–13730, Aug. 2022.

[14] J. M. Schneider and J. J. O'Hare, "Alignment, verification and optimization of high power wireless charging systems," U.S. Patent 2014/0 217 966 A1, Jun. 28, 2012.

[15] W. Ni et al., "Radio alignment for inductive charging of electric vehicles," *IEEE Trans. Ind. Inform.*, vol. 11, no. 2, pp. 427–440, Apr. 2015.

[16] A. Babu and B. George, "An efficient readout scheme for simultaneous measurement from multiple wireless passive LC sensors," *IEEE Trans. Instrum. Meas.*, vol. 67, no. 5, pp. 1161–1168, May 2018.

[17] W. Han, K. T. Chau, C. Jiang, and W. Liu, "Accurate position detection in wireless power transfer using magnetoresistive sensors for implant applications," *IEEE Trans. Magn.*, vol. 54, no. 11, Nov. 2018, Art. no. 4001205.

[18] K. Hwang, J. Cho, J. Park, D. Har, and S. Ahn, "Ferrite position identification system operating with wireless power transfer for intelligent train position detection," *IEEE Trans. Intell. Transp. Syst.*, vol. 20, no. 1, pp. 374–382, Jan. 2019.

[19] Y. Shin, K. Hwang, J. Park, D. Kim, and S. Ahn, "Precise vehicle location detection method using a wireless power transfer (WPT) system," *IEEE Trans. Veh. Technol.*, vol. 68, no. 2, pp. 1167–1177, Feb. 2019.

[20] C. Cai, M. Saeedifard, J. Wang, P. Zhang, J. Zhao, and Y. Hong, "A cost-effective segmented dynamic wireless charging system with stable efficiency and output power," *IEEE Trans. Power Electron.*, vol. 37, no. 7, pp. 8682–8700, Jul. 2022.

[21] L. Wang et al., "Mutual inductance identification of IPT system based on soft-start process," *IEEE Trans. Power Electron.*, vol. 37, no. 6, pp. 7504–7517, Jun. 2022.

[22] T. Hamada, D. Shirasaki, T. Fujita, and H. Fujimoto, "Proposal of sensorless vehicle detection method for start-up current control in dynamic wireless power transfer system," in *Proc. 47th Annu. Conf. IEEE Ind. Electron. Soc.*, 2021, pp. 1–6.

[23] I. Cortes and W. J. Kim, "Lateral position error reduction using misalignment-sensing coils in inductive power transfer systems," *IEEE ASME Trans. Mechatronics*, vol. 23, no. 2, pp. 875–882, Apr. 2018.

[24] J. Li, F. Yin, L. Wang, B. Cui, and D. Yang, "Electromagnetic induction position sensor applied to anti-misalignment wireless charging for UAVs," *IEEE Sensors J.*, vol. 20, no. 1, pp. 515–524, Jan. 2020.

[25] R. Zhang, H. Yao, Z. Cao, W. Zhong, and L. Cao, "A coordinate positioning technique based on region partitioning for EV wireless charging system," *IEEE Trans. Ind. Electron.*, vol. 71, no. 3, pp. 2443–2453, Mar. 2024.

[26] B. Zhang et al., "Triple-Coil-Structure-Based coil positioning system for wireless EV charger," *IEEE Trans. Power Electron.*, vol. 36, no. 12, pp. 13515–13525, Dec. 2021.

[27] Z. Zhang, S. Zheng, Z. Yao, D. Xu, P. T. Krein, and H. Ma, "A coil positioning method integrated with an orthogonal decoupled transformer for inductive power transfer systems," *IEEE Trans. Power Electron.*, vol. 37, no. 8, pp. 9983–9998, Aug. 2022.

[28] D. Patil, J. Miller, B. Fahimi, P. T. Balsara, and V. Galigerkere, "A coil detection system for dynamic wireless charging of electric vehicle," *IEEE Trans. Transp. Electrific.*, vol. 5, no. 4, pp. 988–1003, Dec. 2019.

[29] Z. Liu et al., "Receiver position identification method of wireless power transfer system based on magnetic integration inductance," *IEEE Trans. Ind. Appl.*, vol. 58, no. 1, pp. 1136–1145, Jan. 2022.

[30] C. Cai et al., "Optical fiber composite winding for in situ thermal monitoring of transmitter magnetic mechanism in long-track DWPT systems," *IEEE Trans. Instrum. Meas.*, vol. 73, Nov. 2024, Art. no. 9000604, doi: 10.1109/TIM.2023.3329107.

[31] F. W. Grover, *Inductance Calculations*. New York, NY, USA: D. Van Nostrand, 1946.


**Junhua Wang** (Member, IEEE) was born in Shandong, China, in 1981. He received the Ph.D. degree in electrical engineering from Hong Kong Polytechnic University, Hong Kong, China, in 2012.

He is currently a Professor with the School of Electrical Engineering and Automation, Wuhan University, Wuhan, China. He joined Carnegie Mellon University as a postdoctoral researcher in 2012 and then worked as a research fellow at the GATE Center for Electric Drive Transportation, Michigan, USA. His research interests include wireless transfer technology based on magnetic resonance, applied electromagnetics, and system equipment for power transmission and distribution.

**Leke Wan** received the B.S. degree in transporation equipment and control engineering from Southwest Jiaotong University, Chengdu, China, in 2020. He is currently working toward the Ph.D. degree in electrical engineering with Wuhan University, Wuhan, China.

His research interests include dynamic wireless power transfer, receiver position detection, and multicoil power transmission technology.

**Changsong Cai** (Senior Member, IEEE) received the Ph.D. degree in electrical engineering from Wuhan University, Wuhan, China, in 2020.

From 2019 to 2020, he was a Visiting Researcher with the School of Electrical and Computer Engineering, Georgia Institute of Technology, Atlanta, GA, USA. Since 2021, he has been working with the School of Electrical Engineering and Automation, Wuhan University, Wuhan, China, where he is currently an Associate Professor. His main research focus has been in the area of applied electromagnetics and power electronics, and the research involves power conversion, wireless power transfer, and their applications.

Dr. Cai serves/served as a Guest Associate Editor for IEEE TRANSACTIONS ON POWER ELECTRONICS. He was the recipient of the first place prize paper award from IEEE TRANSACTIONS ON POWER ELECTRONICS in 2022 and an outstanding reviewer award from IEEE TRANSACTIONS ON POWER ELECTRONICS in 2024.

**Ming Xue** was born in Tianjin, China, in 1987. He received the B.S. degree in electrical engineering and automation and M.S. degree in control engineering from Tianjin Polytechnic University, Tianjin, China, in 2011 and 2014, respectively, and the Ph.D. degree in electrical engineering from the Hebei University of Technology, Tianjin, China, in 2022.

He is currently an A.P. with the School of Electrical Engineering, Hebei University of Technology. His research interests include wireless power transfer technology and its application.

**Yinfeng Du** received the B.S. degree in electrical engineering and automation from Sichuan University, Chengdu, China, in 2023. He is currently working toward the M.S. degree in electrical engineering with Wuhan University, Wuhan, China.

His research interests include wireless power transfer and its industrial applications.

**Jin Zhang** received the B.S. degree in electrical engineering and automation from Hefei University of Technology, Hefei, China, in 2021. He is currently working toward the M.S. degree in electrical engineering with Wuhan University, Wuhan, China.

His research interests include wireless power transfer and its industrial applications.